Astronomy Letters, Vol. 26, No. 6, 2000, pp. 379–389. Translated from Pis'ma v Astronomicheskiĭ Zhurnal, Vol. 26, No. 6, 2000, pp. 444–455.

Porous Dust Grains in the Shells of Herbig Ae/Be Stars

V. B. Il'in[1]* and N. A. Krivova[1, 2]

[1] *Astronomical Institute, St. Petersburg State University, Bibliotechnaya pl. 2, Petrodvorets, 198904 Russia*
[2] *Max Planck Institute of Aeronomy, Katlenburg-Lindau, Germany*

Received September 24, 1999; in final form, December 20, 1999

Abstract—The transfer of polarized radiation in inhomogeneous circumstellar shells with a spheroidal spatial distribution of porous dust particles is computed. The grains are modeled by an MRN mixture of silicate and graphite particles. The optical properties of porous particles (considered separately in the Appendix) are computed by using effective medium theory and Mie theory. The following observational characteristics have been computed for WW Vul, a typical Herbig Ae star with Algol-like minima: the spectral energy distribution from the ultraviolet to the far infrared, the color–magnitude diagrams, the wavelength dependence of linear polarization, and the shell brightness distribution. The effect of grain porosity on the results is considered. It has been found that only moderate particle porosity (the volume fraction of matter is f ~ 0.5) can explain available observational data in terms of the approach used. Since radiation pressure must rapidly sweep submicron-sized grains out of the vicinity of Herbig Ae/Be stars, we briefly discuss how particle porosity can affect this process. © *2000 MAIK "Nauka/Interperiodica".*

Key words: *stars—circumstellar shells, interstellar dust*

1. INTRODUCTION

Herbig Ae/Be (HAeBe) stars are young stars of moderate mass (2–8 $M_\odot$), which appear to be the precursors of Vega- and β Pic-type main-sequence stars surrounded by gas–dust protoplanetary disks. Considerable infrared (IR) excesses commonly observed in HAeBe stars are generally explained by thermal dust radiation. However, it is unlikely that dust particles can form in the shells of these stars, while strong radiation pressure makes it difficult for dust grains to exist near the stars for long. Circumstellar dust is assumed to be the remnant of a protostellar cloud and is continuously supplied to the inner shell layers by comet-like bodies [1]. The presence of dust around Vega- and β Pic-type stars can be explained in a similar way [2, 3].

When modeling the shells around HAeBe stars, only compact dust particles have always been considered (see, e.g., [4–8]). Meanwhile, many of the existing models for interstellar dust suggest a certain grain porosity (see [9] and references therein). Note that the hypothesis of particle porosity in the disk around β Pic allows available observational data to be interpreted in a more consistent way [10, 11]. The presumably low albedo of circumstellar particles [12] can also be evidence that the dust grains in the vicinity of HAeBe stars are not compact.

Here, we consider the influence of particle porosity on the observational manifestations of circumstellar dust: the IR spectrum, the circumstellar extinction curves, the color variations during brightness minima (for UX Ori-type HAeBe stars), the wavelength dependence of polarization, and the shell brightness distribution. Our shell model and the representation of porous dust grains in it are described in Section 2; the results of our calculations are presented and discussed in Section 3. The Appendix contains figures that show how porosity affects the optical properties of silicate and graphite particles of difference sizes.

2. MODEL

2.1. Porous Dust Grains

To describe the optical properties of circumstellar dust grains, we used the MRN model by Mathis *et al.* [13], to which we added one more parameter, particle porosity p (the fraction of the particle volume occupied by vacuum). Thus, two types of dust grain were assumed to be simultaneously present in the shell: graphite and silicate ones. Both are spherical and have the same power-law size distribution

$$n(a) \sim a^{-q}, \quad (1)$$

* E-mail address for contacts: vi2087@vi2087.spb.edu

where q is a constant. The model parameters also include the largest and smallest particle sizes, $a_{\min}$ and $a_{\max}$, as well as the ratio (by number) of silicate particles to graphite ones, n_{Si}/n_C. Here, we do not discuss advantages and disadvantages of the MRN model. Note only that this is one of the existing models for interstellar dust, with each having its own difficulties in explaining the entire set of available direct and indirect data on interstellar grains (see, e.g., [14, 15]). Nevertheless, it is the MRN model that has been used virtually always in calculations similar to ours.

We determined the optical properties of porous grains by using effective medium theory (EMT) and Mie theory. In other words, a porous particle was replaced by a compact homogeneous sphere with some mean refractive index $\langle m \rangle$. The latter was calculated by using Bruggeman's rule [16]

$$(1-p)\frac{m_1^2 - \langle m \rangle^2}{m_1^2 + 2\langle m \rangle^2} + p\frac{m_0^2 - \langle m \rangle^2}{m_0^2 + 2\langle m \rangle^2} = 0, \qquad (2)$$

where m_1 is the refractive index of silicate or graphite (in both cases, the refractive indices were taken from [17]), and $m_0 = 1$ is the refractive index of vacuum. Note that EMT has a wide range of applicability (see, e.g., [16, 18, 19]).

Some optical parameters of silicate and graphite particles that we calculated by using EMT and Mie theory are shown in the figures in the Appendix. The optical properties of the MRN grain aggregates considered here can also be inferred from them.

2.2. Dust Distribution in the Shell

The dust in the shell was assumed to have a spheroidal spatial distribution,

$$n(\mathbf{R}) = n_0[\sqrt{R_x^2 + R_y^2 + R_z^2(A/B)^2}]^{-\alpha}, \qquad (3)$$

where R_x, R_y, R_z are the coordinates of radius vector $\mathbf{R}$, A/B is the flattening (axial ratio) of spheroidal equidensites, and n_0 and α are constants. The angle between the line of sight and the equidensite symmetry axis is i.

There is a dust-free spherical zone of radius R_{in} at the shell center. We determined R_{in} by taking into account the fact that the temperature of the grains at this distance from the star cannot exceed their sublimation temperature (about 1500 K). The outer radius R_{out} of the dust shell was chosen to be constant (4.7×10^3 AU). Its value affects weakly the radiation fluxes in the spectral range under consideration ($\lambda < 100$–300 μm).

We emphasize that, although the shell in our model is spherical, its dust distribution is not spherically symmetric. For this reason, the total radiation emerging from the shell is polarized, and the degree of its polarization depends on A/B and on other model parameters.

2.3. Method of Calculation

We computed the transfer of polarized radiation in the shell by the Monte Carlo method using the program developed by Fischer [20].

The grain temperatures at various distances from the star required for such calculations were determined for a simplified shell model with a spherically symmetric dust distribution,

$$n(R) = n_0' R^{-\alpha} \qquad (4)$$

and with the same sizes and mass as those of the shell with the spherodical distribution given by (3). This approximation is accurate enough (see, e.g., [21]). Below, the shell models with the dust distributions given by (3) and (4) are called, respectively, spheroidal (or two-dimensional) and spherically symmetric (or one-dimensional).

We simulated the transfer of unpolarized radiation in the spherically symmetric shell by using Kruegel's program described in [22]. The changes required to realize the chosen model were made to both programs (see [21] for more detail).

2.4. Brightness Minima

Several HAeBe stars (UX Ori, WW Vul, etc.) exhibit Algol-like minima, which are accompanied by characteristic color and polarization variations [23, 24]. In the currently most popular hypothesis, the minima of UX Ori-type stars are associated with eclipses of the stars by circumstellar clumps of gas and dust ([24, 25]; see, however, [26]). As a result, at minimum light, the fraction of the radiation scattered in the shell increases, and, hence, the star + shell system becomes bluer, while the degree of linear polarization increases, in general agreement with observations (see [24] and references therein).

Clearly, the observed color and polarization variations in this hypothesis must be determined mainly by the properties, amount, and distribution of circumstellar dust in the inner shell layers. Recall that the same layers give a major contribution to the IR spectrum (except the far infrared) and to circumstellar extinction and scattering. We therefore modeled both the spectral energy distribution and the color and polarization variations in terms of the hypothesis described above. Simple relations, for example, those from [27, 28], were used to calculate the latter.

3. RESULTS OF THE CALCULATIONS AND THEIR DISCUSSION

Here, we did not set the objective of comprehensively interpreting the observational data for a specific HAeBe star listed in the Introduction. Instead, we chose a typical shell model and varied the grain porosity in it. Subsequently, a comparison of the results for shells with the same sizes (and optical depths for visi-

ble absorption τ_V^{abs}) revealed the main effects of grain noncompactness.

We chose the model of the shell around WW Vul proposed by Friedemann *et al.* [29] as the basic model. This model is well developed and satisfactorily accounts for the observed IR spectrum. Other models of this dust shell have similar parameters [7, 28].

3.1. Spectral Energy Distribution

Figure 1 shows our computed spectral energy distributions for the spherically symmetric (one-dimensional) model of the shell around WW Vul ($T_* = 9500$ K, $L_* = 80\,L_\odot$)) at various circumstellar particle porosities ($p = 0$, 0.3, and 0.6). The model parameters $R_{in} = 2.7$ AU, $R_{out} = 4.7 \times 10^3$ AU, $\alpha = 1.45$, $n_{Si}/n_C = 1.12$, $q = 3.5$, $a_{min} = 0.005$ μm, and $a_{max} = 0.32$ μm were fixed; only n_0 was varied with p to keep the optical depth τ_V^{abs} constant, which allowed us not to violate satisfactory agreement between the observed and theoretical IR spectra. Note that varying A/B alone affects weakly the shape of the IR spectrum for shells of the same mass [21]. In general, the variations in the above parameters of the spherically symmetric shell are also insignificant if τ_V^{abs} is constant [12, 30].

It is easy to see that, as the grain porosity p increases from 0 to 0.6, the peak in the IR spectrum, while maintaining its magnitude, shifts longward (from 2.5 to 4.5 μm), and a dip is formed in the energy distribution at $\lambda \approx 1.5$–2 μm. In addition, the emission bands at λ 10 and 20 μm become less distinct, and the spectral slope in the far infrared ($\lambda > 60$ μm) slightly decreases. These spectrum transformations are mainly attributable to changes in the grain temperature and in the relative contribution of graphite and silicate particles to the object's IR radiation as the grain porosity increases.

Note that, as p increases further from 0.7 to 0.97, the peak in the IR spectrum is enhanced and shifts shortward (from 4.5 to 2.5 μm). In this case, the dip in the spectrum at $\lambda \approx 1.5$–2 μm is preserved, while the intensity of the emission bands at λ 10 and 20 μm slightly increases. The change in the behavior of the curves at $p \approx 0.6$–0.7 results from an abrupt change in the optical properties of porous graphite particles in the infrared (cf. Figs. 6 and 7 in the Appendix).

Recall that porous grains are more or less compact particles with insignificant vacuum inclusions for $p \longrightarrow 0$ and most likely an assembly of small subparticles for $p \longrightarrow 1$ (see, e.g., [31]). The optical properties of silicate and graphite particles vary with p differently, at least in the EMT approximation (see Figs. 6–9 in the Appendix), and, as a result, the pattern of variations in the grain temperature and, consequently, in the emission spectra with porosity proves to be fairly complex for the MRN mixture of particles.

The far-IR shell spectrum is mainly determined by Q_{abs}/a, where Q_{abs} is the absorption efficiency, and a is the grain size. Variations of Q_{abs}/a with particle porosity p have been repeatedly considered previously (see, e.g., [32]), while the influence of grain porosity on the profile of the λ 10 μm silicate band was discussed by Hage and Greenberg [31] and Henning and Stognienko [33] (see also Fig. 8 in the Appendix).

Note also that, if we fix all shell parameters except p and n_0, then the mass of the circumstellar dust, which gives approximately the same IR flux, first decreases with increasing p and then increases (a minimum at $p \approx 0.6$–0.7). For example, for a shell with the parameters from Subsection 3.1, the IR flux is approximately the same at $M_{sh} = 6.6 \times 10^{-6}\,M_\odot$ (for $p = 0$), $3.9 \times 10^{-6}\,M_\odot$ ($p = 0.65$), $8.3 \times 10^{-6}\,M_\odot$ ($p = 0.97$), etc. Such an effect was noted by Mathis [34] when searching for a minimum of the dust mass required to explain the observed interstellar extinction in the Galaxy.

The behavior of the ultraviolet (UV) spectrum can be better traced in Fig. 2, which shows the so-called circumstellar extinction curve—the wavelength dependence of extinction in the shell. Note that the extinction in this case is defined as the difference between the flux from the object (star + shell) and the flux from the star without a shell and differs from the extinction by dust on the line of sight [6].

Since the circumstellar extinction curve is not known for WW Vul, Fig. 2 shows the results obtained from the observations of the star NX Pup by Tjin A Djie *et al.* [35]. NX Pup ($T_* = 9500$ K, $L_* = 100\,L_\odot$) closely resembles WW Vul, and its circumstellar extinction curve is more or less typical of HAeBe stars (see, e.g., the curve for AB Aur in [4]).

As we see from Fig. 2, the peak at λ2200 Å weakens and shifts longward as p increases from 0 to 0.6. As p increases further (from 0.7 to 0.97), a significant change occurs, as in the case of the IR spectrum: the peak is enhanced and shifts shortward, with the rise in the far ultraviolet ($1/\lambda > 6.2\ \mu m^{-1}$) becoming very steep (see Fig. 8 in the Appendix). Note, however, that these results must be treated with caution. It is unclear whether EMT is applicable to those cases where the size of particle inhomogeneities is comparable to or larger than the wavelength of the radiation, which is quite possible in the far ultraviolet.

3.2. Color–Magnitude Diagrams

Figure 3 shows our computed diagrams for the photometric U, B, V, R, and I bands. For comparison, we present the results of observations for WW Vul at one of the minima [36].

We found the theoretical curves to monotonically displace downward and to the right as p increases; this tendency is also preserved for $p > 0.6$. This is because an increase in grain porosity, with the grain size being preserved, usually causes the albedo to decrease (see,

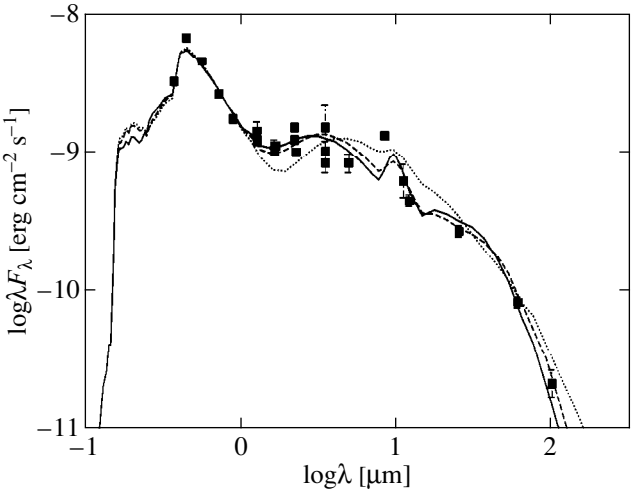

Fig. 1. Spectral energy distributions for a spherically symmetric model of the shell around WW Vul at various grain porosities: $p = 0$ (solid line), $p = 0.3$ (dashed line), and $p = 0.6$ (dotted line). The squares represent observational data from [54–58].

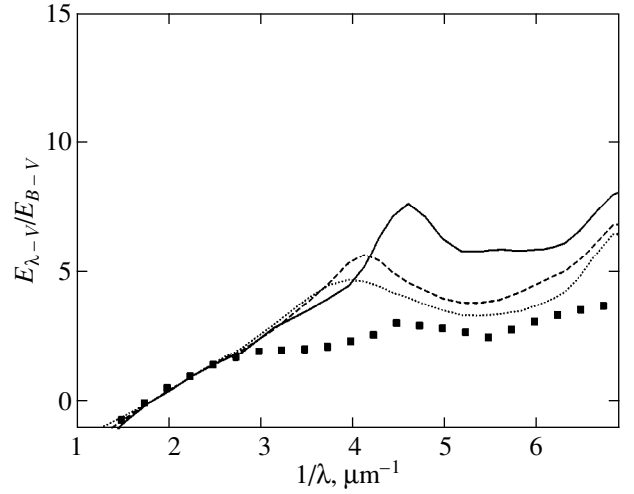

Fig. 2. Circumstellar extinction curves for a spherically symmetric model of the shell around WW Vul at various grain porosities. The notation is the same as in Fig. 1. The squares represent data for NX Pup from [35].

e.g., [31] and Fig. 9 in the Appendix). At the same time, the ensemble-averaged grain albedo $\langle\Lambda\rangle$ determines the fraction of the scattered radiation in the object's total radiation (for optically thin shells). For the same thermal radiation, porous grains therefore scatter starlight worse than do compact particles; accordingly, the star tracks in the color–magnitude diagram are less deformed, i.e., deviate less from the initial straight lines that they must be in the absence of scattered radiation.

For compact grains ($p = 0$), the theoretical curves run well away from the observational points, which we pointed out in [12]. We also showed that the problem could be solved if $\langle\Lambda\rangle \approx 0.3$–$0.4$ in the visible range. Recall that interstellar grains and, consequently, the standard MRN mixtures used for their representation have $\langle\Lambda\rangle \approx 0.5$–$0.7$ (see, e.g., [37]).

Circumstellar-particle porosity can explain the low albedo in a natural way. However, there are also other possibilities to achieve agreement between the theoretical and observed spectra and diagrams simultaneously, for example, by attributing ~50% of the observed near-IR flux that we did not took into account to the radiation of gas and/or very small grains (see, e.g., [38, 39]) or by assuming that the dust in the shell concentrates mainly in optically thick clumps [40, 41]. In addition, for shells without spherical symmetry, the ratio of the total scattered flux to the thermal flux from circumstellar dust can depend strongly not only on the mean particle albedo, as was shown above, but also on the shell orientation relative to the observer (inclination i). Recall that the fraction of the scattered light emerging from an optically thin oblate shell in the direction of the equatorial plane is usually larger than that from the poles, because the scattering is anisotropic and because the dust distribution is nonspherical (see, e.g., [42]). When a spheroidal shell is observed at different inclinations i to the symmetry axis, the scattered flux therefore increases with i, while the thermal flux, which is essentially isotropic, is preserved.

When the grains scatter radiation only forward, i.e., when the asymmetry factor of the phase function is $\langle\cos\Theta\rangle = 1$, the following simple relation clearly holds for the i dependence of the total scattered flux emerging from a shell with the dust distribution (3) toward the observer:

$$F_{\rm sh}(i) = F_{\rm sh}(90)\left[\sin^2 i + \left(\frac{A}{B}\right)^2\cos^2 i\right]^{-\alpha/2}. \qquad (5)$$

It shows that, for very oblate shells ($A/B \gg 1$) observed nearly edge-on ($i \sim 90°$), the dependence of $F_{\rm sh}$ on i must be appreciable, $F_{\rm sh}(i) \sim \left(\frac{\pi}{2} - i\right)^{-\alpha}$, because α is expected to be ~1.5–2. The flux ratio is $F_{\rm sh}(0)/F_{\rm sh}(90) = (A/B)^{-\alpha}$ and differs markedly from 1.

The asymmetry factor of the phase function $\langle\cos\Theta\rangle$ for particles of the MRN mixture in the visible range is close to 1, and formula (5) can be of use. Our calculations confirm that, in general, the dependence of $F_{\rm sh}$ on i follows relation (5), although $\langle\cos\Theta\rangle < 1$ and the optical depth $\tau \sim 1$.

It should be noted that the effect of orientation of a nonspherical shell relative to the observer clearly cannot be invoked to account for the difficulty in simultaneously interpreting the IR spectra and the color–magnitude diagrams (the "excess" scattered flux in models). It can hardly be assumed that only shells seen at an angle to their equatorial plane (for example, $|90° - i| > 20°$) and, hence, with a deficit of scattered radiation are observed. For a random distribution of the shell symmetry planes in space, the number of shells seen nearly

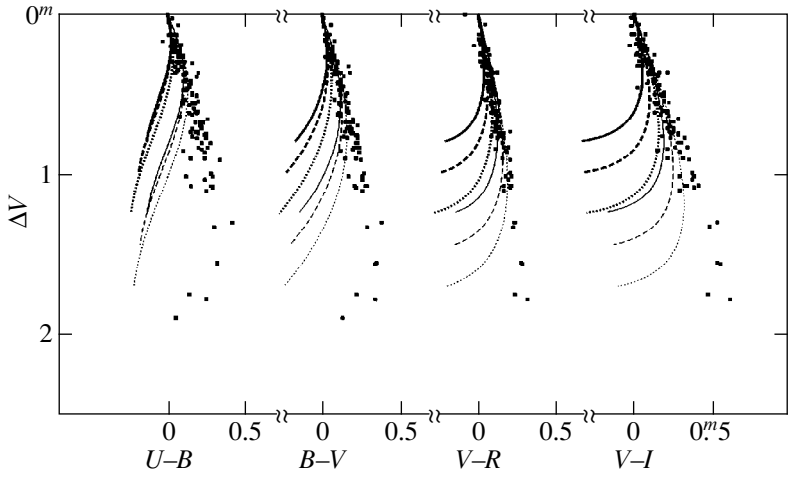

Fig. 3. Color–magnitude diagrams for the *UBVRI* bands for a spheroidal model of the shell around WW Vul. The heavy and normal lines are for inclinations $i = 90°$ and 70°, respectively; the remaining notation is the same as in Fig. 1. The squares represent observational data for WW Vul at minimum light from [36].

edge-on ($|90° - i| < 10°$) and, consequently, without this deficit must always be significant.

Note, on the other hand, that the scattered-to-stellar flux ratio F_{sh}/F_* determines the position of the turning point of the star track in the color–magnitude diagram (see [12]). At large A/B, F_{sh}/F_* depends strongly on i [see, e.g., formula (5)], and the tracks must turn at markedly different levels of brightness decline (ΔV) for different stars. If the tracks for a large group of UX Ori-type objects had been available, then we could have inferred the flattening of their scattering dust shells (spherical or disk-like ones).

3.3. Linear Polarization

Although the linear-polarization variations in the object (star + shell) observed during minima are considerable, they are satisfactorily described by the following approximate relation [36]:

$$\mathbf{P}_{obs}(\Delta m) \approx \mathbf{P}_{is} + \mathbf{P}_{sca} \times 10^{0.4\Delta m}, \qquad (6)$$

where Δm is the change in magnitude; and $\mathbf{P}_{obs}$, $\mathbf{P}_{is}$, and $\mathbf{P}_{sca}$ denote, respectively, the object's observed polarization, the interstellar polarization (including the polarization produced by dust extinction on the line of sight in the shell), and the polarization produced by the scattered radiation of the shell. The latter can be represented as

$$P_{sca} = \frac{\sqrt{Q_{sh}^2 + U_{sh}^2}}{I_{tot}(\Delta m = 0)} = P_{sh}\frac{I_{sh}}{I_{tot}(\Delta m = 0)}, \qquad (7)$$

where I_{sh}, Q_{sh}, and U_{sh} are the Stokes parameters for the scattered radiation emerging from the shell; $P_{sh} = \sqrt{Q_{sh}^2 + U_{sh}^2}/I_{sh}$, $I_{sh}/I_{tot}(\Delta m = 0)$ is the fraction of the scattered radiation in the object's total radiation at maximum light; and $I_{tot}(\Delta m = 0) = I_* \exp(-\tau^{ext}) + I_{sh}$, where I_* is the stellar radiation, and τ^{ext} is the optical depth of the shell for absorption (along the line of sight).

The wavelength dependence of linear polarization $P_{sca}(\lambda)$ can give additional important information about the properties of circumstellar dust. The curves in Fig. 4 indicate this dependence computed for models with $A/B = 5$ at various grain porosities ($p = 0$, 0.3, and 0.6). Note that P_{sca} monotonically decreases as the porosity increases further ($p > 0.6$). The points in Fig. 4 represent the values taken from [36], where they were determined from the observed values by using relation (6).

It should be noted that, although the computed P_{sca} are in satisfactory agreement with the observed ones (see Fig. 4), the polarization of the scattered radiation from the shell P_{sh} at $p \approx 0$–0.3 turns out to be considerably smaller than its estimates that can be obtained from observations. The reason is that the theoretical ratio $I_{sh}/I_{tot}(\Delta m = 0)$ in formula (7) is clearly overestimated for models with such porosities p, as the corresponding tracks in the color–magnitude diagram show (see Fig. 3).

The case of a shell with $A/B = 5$ we chose corresponds to a nearly maximum P_{sh} [21, 42]. Since P_{sh} rapidly decreases with p (for $p > 0.7$), we conclude that models with a large particle porosity can hardly explain the observed polarization in UX Ori-type stars.

Shells with a disk-like dust distribution (for example, a dust disk in the shape of a sphere without polar cones, which one might expect when a magnetic field does not govern the motion of grains, and they are swept out of the inner shell layers almost radially by stellar radiation) can have a slightly higher degree of polarization P_{sh}. Nevertheless, our estimates show that no disk-like dust distribution (for the representation of porous grains we used) can give a considerably larger

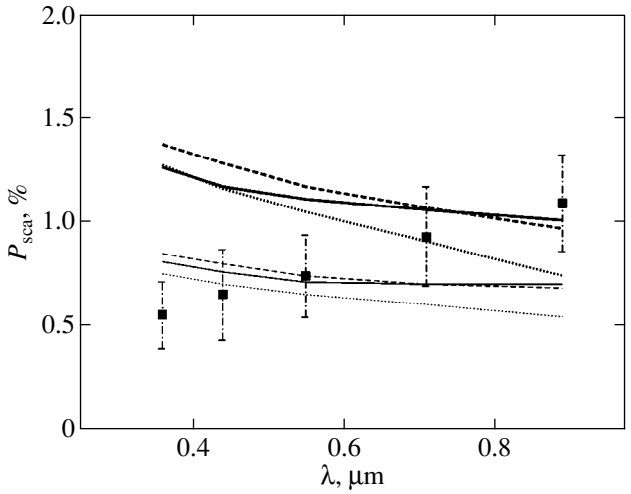

Fig. 4. Wavelength dependence of linear polarization for a spheroidal model of the shell around WW Vul. The notation is the same as in Fig. 3. The squares represent data for WW Vul from [36].

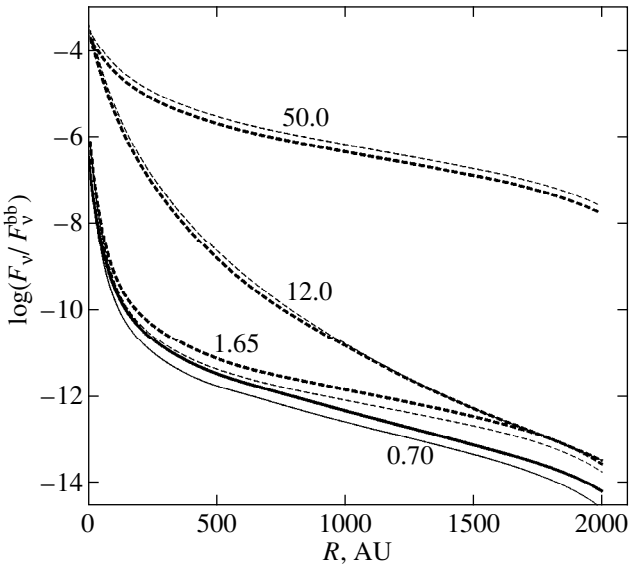

Fig. 5. Brightness distributions at various wavelengths for a spheroidal model of the shell around WW Vul. The heavy and normal lines are for $p = 0$ and 0.6, respectively. F_ν^{bb} is the flux from a blackbody of temperature $T_* = 9500$ K.

P_{sh} than that for the very oblate spheroidal shells we considered and can thus explain the results of our observations.

3.4. Shell Brightness Distribution

To the best of our knowledge, as yet no sufficiently detailed maps of the brightness distribution have been obtained for the shells of HAeBe stars with minima; however, they should be considered as observational tests, which will be possible in the near future. Figure 5 shows the brightness distributions at several wavelengths ($\lambda = 0.7$, 1.65, 12, and 50 μm) computed for two models with particle porosities $p = 0$ and 0.6. The fluxes from the peripheral regions of the shells with porous grains are seen to be a factor of 3–5 lower than those for the shells with compact grains. This is because the phase function for porous particles is generally more elongated forward than that for compact particles (see, e.g., [43] and Fig. 9 in the Appendix).

Polarization maps with a sufficiently high spatial resolution are unlikely to be obtained for UX Ori-type stars in the immediate future. We therefore do not provide and do not discuss here our computed distributions of the polarization parameters over the shell image. Note that they are mainly determined by other parameters than the porosity of circumstellar dust particles (see [44] for more detail).

3.5. Radiation Pressure on Dust

It should be noted that the mere assumption that comet-like bodies supply grains to the inner shell layers does not yet completely solve the problem of submicron-sized grains being present in them—the radiation pressure of HAeBe stars is strong enough to set such a high rate of dust outflow from the shell that it cannot be offset even by the complete breakup of all comet-like bodies near the star [45]. A magnetic field of a certain geometry can slow down the sweeping out of charged grains but cannot change radically the situation [46]. It is therefore of interest to consider how grain porosity can affect the efficiency of their sweeping out of the vicinities of HAeBe stars.

The effect of particle porosity on the radiation-pressure force was discussed in detail by Mukai *et al.* [47] for a rather peculiar model of circumsolar dust grains (fractal aggregates of subparticles). We consider this effect in terms of the representation of porous grains used.

The radiation-pressure force is known to be

$$F_{pr} = \frac{1}{c}\frac{R_*^2}{R^2}\sigma T_*^4 \bar{C}_{pr}, \qquad (8)$$

where $\bar{C}_{pr}$ is the flux-averaged radiation-pressure cross section, R_* and T_* are the stellar radius and temperature, R is the distance from the star to the particle, c is the speed of light, and σ is the Stefan–Boltzmann constant. For silicate and even for graphite at $p > 0.5$, the effective complex refractive index is $(\langle m\rangle - 1) \sim f$, where $f = 1 - p$ is the filling factor of a porous grain. For $x = 2\pi a/\lambda < 0.1$–1, which includes a substantial part of the integration range when averaging the cross section in (8), $C_{pr} \approx 16\pi^2 a^3 \mathrm{Im}(\langle m\rangle - 1)/(3\lambda) \sim a^3 f$, where λ is the wavelength of the incident radiation. Thus, the radiation-pressure force is approximately the same for particles of the same mass but of different porosity and rapidly

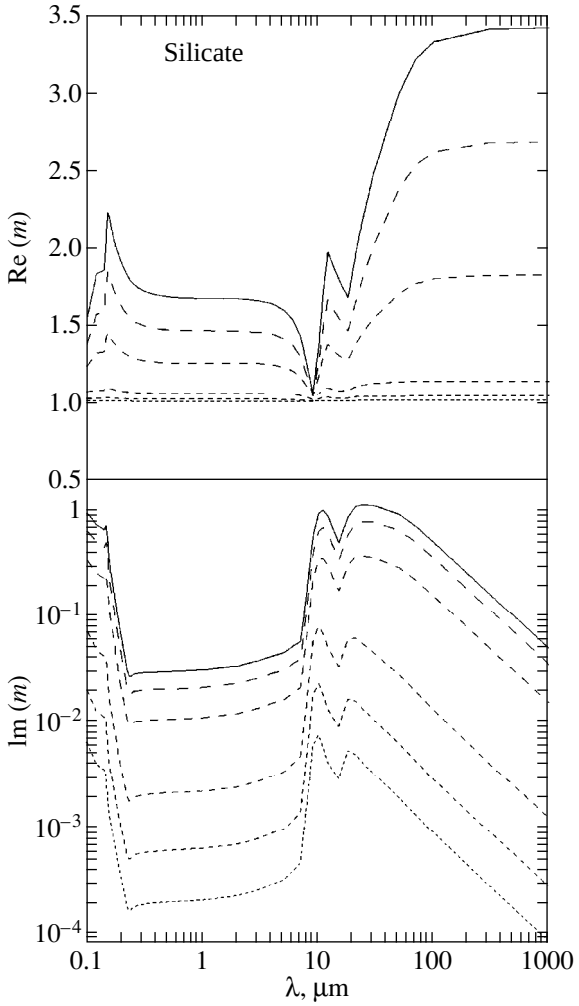

Fig. 6. Complex refractive index m for mixtures of astronomical silicate with vacuum. The porosities are $p = 0$ (solid lines), 0.3, 0.6, 0.9, 0.97 (dashed lines), and 0.99 (dotted lines).

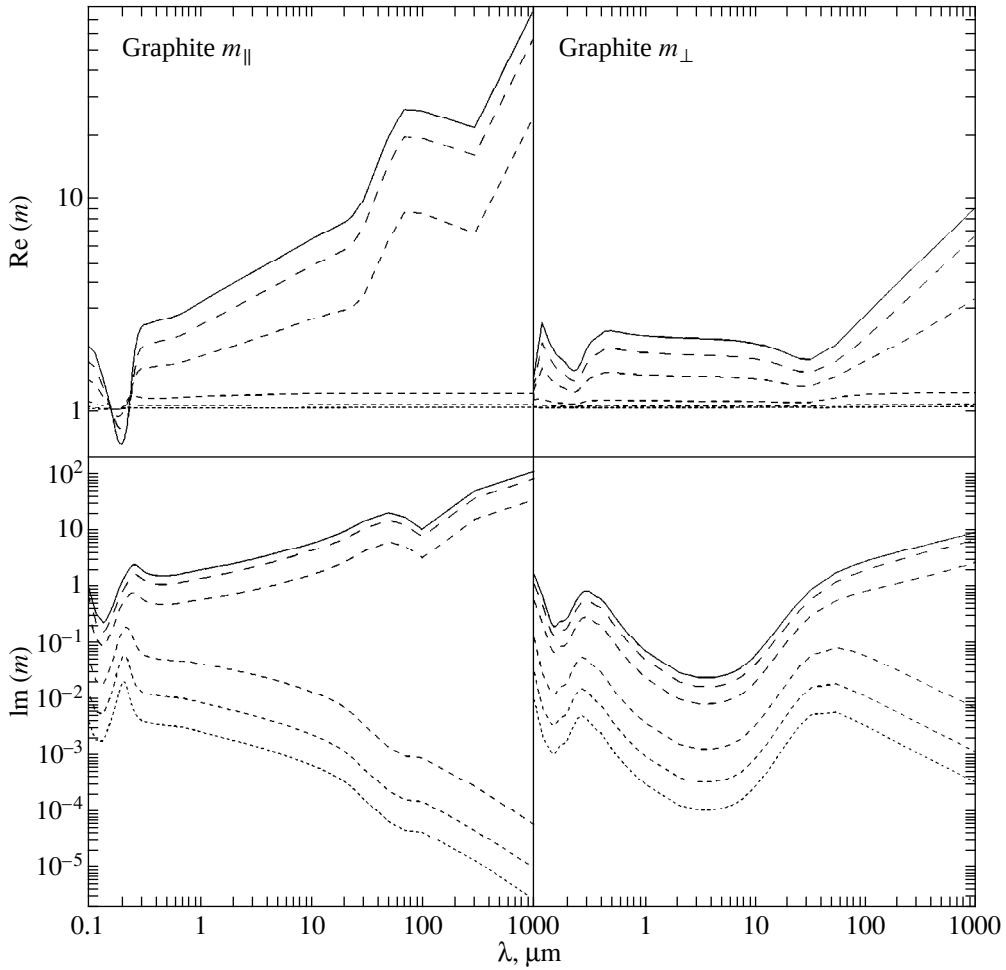

Fig. 7. Same as Fig. 6 for graphite in the case of m = $m_{\parallel}$ and $m = m_{\perp}$.

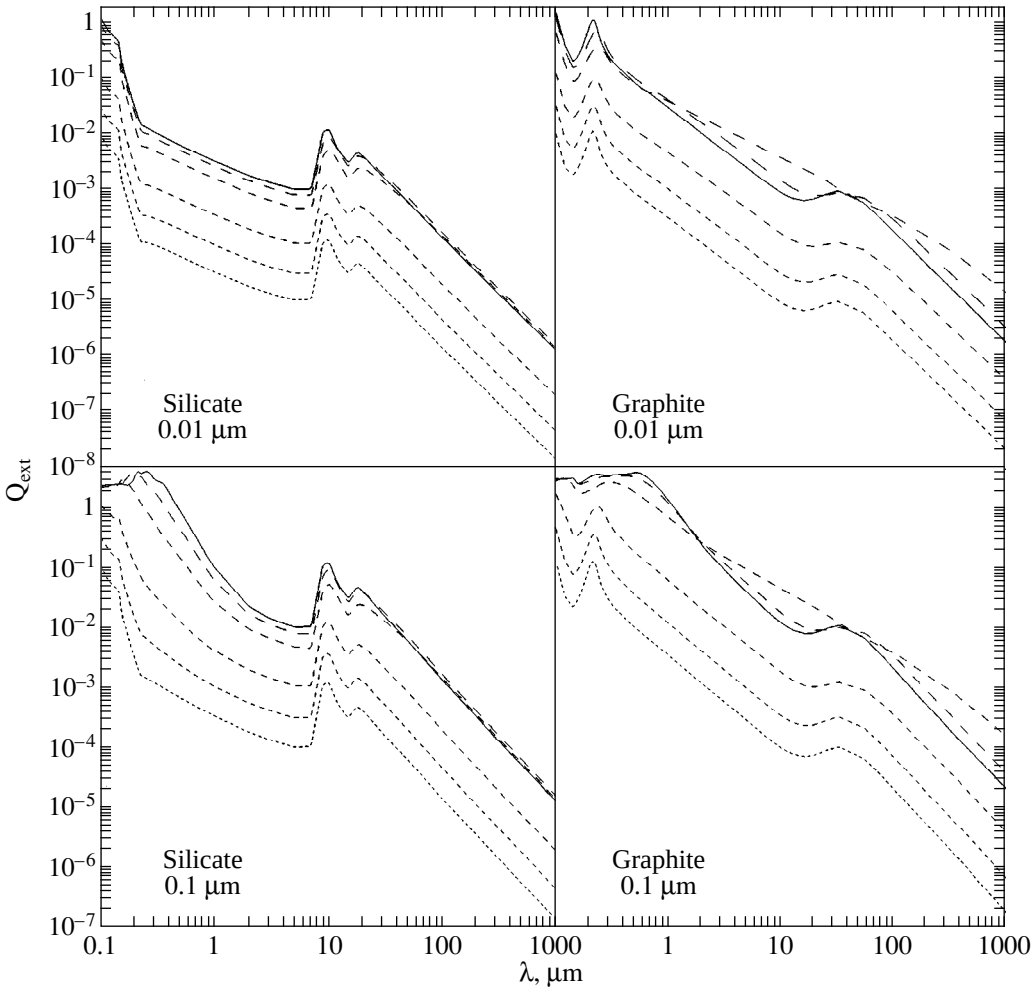

Fig. 8. Extinction efficiencies Q_{ex} for silicate and graphite porous particles of size 0.01 and 0.1 μm.

decreases with increasing p (or decreasing f) for particles of the same size.

An important dynamic indicator is the ratio of radiation-pressure force F_{pr} to gravitational force F_g,

$$\beta = \frac{F_{pr}}{F_g} = \frac{3\sigma}{4\pi c\gamma}\frac{R_*^2 T_*^4}{M_*}\frac{\bar{C}_{pr}}{\rho a^3 f}, \qquad (9)$$

where ρ is the density of the grain material, M_* is the stellar mass, and γ is the gravitational constant. If $\bar{C}_{pr} \sim a^3 f$ (see above), then β does not depend on the grain size and porosity.

We computed Planck mean radiation-pressure cross sections and β for an A0 star ($R_* = 2.5\ R_\odot$; $T_* = 10^4$ K, $M_* = 3.2\ M_\odot$). At large particle porosity and for $a < 0.1$–0.3 μm, β was found to be almost independent of the grain size and roughly correspond to its values for very small, compact grains ($a < 0.001$ μm). For $a > 0.3$–1 μm, β rapidly decreases with increasing a. Recall that, by contrast, there is a noticeable peak of the dependence $\beta(a)$ at $a \sim 0.01$–0.2 μm for compact particles (see, e.g., [48]).

Note also that, for $p \sim 0.9$ and $a < 0.3$ μm, we obtained $\beta \approx 6$–7 and $\beta \sim 70$ for silicate and graphite porous particles, respectively. Although allowance for the star's actual spectral energy distribution must slightly reduce β (see, e.g., [49]), we conclude that even the large porosity of submicron-sized grains composed of astronomical silicate or of more absorptive materials (graphite, amorphous carbon, iron oxide, etc.) cannot prevent their sweeping out of the vicinities of HAeBe stars. Only porous particles of any size composed of less contaminated silicates than astrosil (see, e.g., [50]) can have $\beta < 1$. However, the albedo of such grains is large, and they cannot simultaneously explain the observed IR fluxes and color–magnitude diagrams (at least in terms of the approach used here).

4. CONCLUDING REMARKS

We considered the transfer of polarized radiation in shells with a spheroidal dust distribution at various

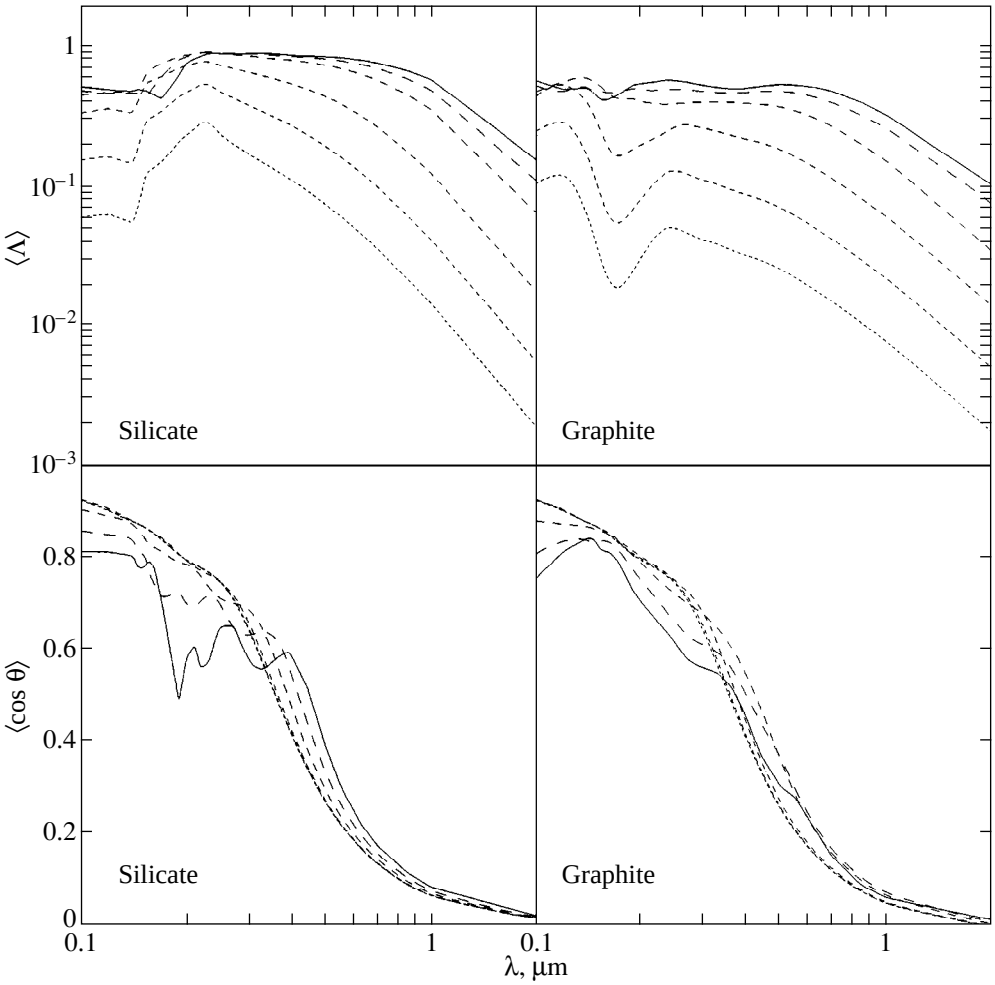

Fig. 9. Albedo and the asymmetry factor of the phase function for silicate and graphite porous particles of size 0.1 μm.

grain porosities. We revealed the effects of noncompactness of circumstellar particles on the observational manifestations of dust shells around HAeBe stars: the spectral energy distribution from the ultraviolet to the infrared, the color–magnitude diagram in the visible range, the wavelength dependence of linear polarization, and the shell brightness distribution in the plane of the sky.

We showed that, in the model we chose, agreement with observational data could be achieved only for grains with a moderate porosity ($p \sim 0.5$). Such a porosity is postulated in some currently available models of interstellar dust (see, e.g., [15]). A considerably larger particle porosity $p \sim 0.9$ is commonly assumed for the grains around β Pic-type stars and of cometary dust [11].

Note that the MRN mixture of particles that we used in our modeling is not quite natural when porous grains are considered. Clearly, the latter must most likely result from subparticle coagulation in the interstellar medium, and, thus, the separate existence of porous silicate and porous graphite particles seems unjustified [15]. We chose the MRN mixture for our analysis, because most similar calculations are performed precisely with this mixture, but the revealed effects must generally show up also for a different representation of an assembly of circumstellar grains. We consider the porosity effects for several models of the particles in the shells of HAeBe stars in the next paper [44].

Here, we determined the optical properties of porous dust grains by using the EMT approximation. The latter suggests that the filling factor f does not vary inside the grain. Meanwhile, a more complex case where f generally decreases outward toward the grain edge is realized in many situations, for example, for fractal particles, including such popular ballistic aggregates as BPCA and BPPA. The optical properties of such aggregates have been repeatedly considered previously (see, e.g., [51, 52]). They differ from homogeneous grains in that the asymmetry factor of the phase function $\langle\cos\Theta\rangle$ for them is larger than that for the particles we considered [43]. As a result, the radiation pressure on such aggregates must be slightly lower, and the dependence of the scattered flux on i must be stronger. In order to assess the importance of these effects,

we plan to also compute radiative transfer in the case where circumstellar grains are ballistic aggregates.

ACKNOWLEDGMENTS

We wish to thank E. Kruegel and O. Fischer, who kindly provided the programs for computing the transfer of unpolarized and polarized radiation. We are also grateful to N.V. Voshchinnikov and H. Kimura for their remarks and helpful discussions. One of us (V.I.) was supported by a scientific grant from the Volkswagen company (Germany), as well as the Federal Program "Astronomy" and the Program "Universities of Russia–Basic Research" (project no. 2154).

APPENDIX

The effect of particle porosity on the observational manifestations of polydisperse assemblies of silicate and graphite circumstellar grains is by no means always clear. For a better understanding of this effect, we provide several figures, which show how porosity changes the optical properties of silicate and graphite particles of different sizes. All calculations were performed by using the EMT approximation and Mie theory.

The input data—the effective refractive indices $\langle m \rangle$ calculated by using the rule (2) for various porosities (p = 0–0.99) of astronomical silicate and graphite—are shown in Figs. 6 and 7, respectively. Note the significant change in the wavelength dependence of the imaginary part of refractive index $\langle m \rangle$ for graphite at $p \sim 0.6$–0.7.

The extinction efficiencies Q_{ext} for silicate and graphite particles of size 0.01 and 0.1 μm are shown in Fig. 8. In the infrared ($\lambda >$ 3–10 μm), Q_{abs} have approximately the same wavelength dependence as Q_{ext}. For graphite particles, we applied the so-called $\left(\frac{1}{3} + \frac{2}{3}\right)$ approximation, which uses the relation $Q_{ext} = \frac{1}{3} Q_{ext}(m_{\|}) + \frac{2}{3} Q_{ext}(m_{\perp})$, where $m_{\perp}$ and $m_{\|}$ are the refractive indices of graphite for two orientations of the electric vector of the incident radiation relative to the axis of the hexagonal structure of crystalline graphite (see [53]). This approximation makes it possible to properly allow for the optical anisotropy of graphite for randomly oriented spherical particles. Notice the different behavior of the curves for silicate and graphite over the entire wavelength range at a moderate particle porosity ($p \le 0.6$).

The albedo and the asymmetry factor of the scattering indicatrix for silicate and graphite porous particles of size 0.1 μm are shown in Fig. 9. The behavior of the curves does not change dramatically with particle size.

REFERENCES

1. N. V. Voshchinnikov and V. P. Grinin, Astrofizika **34**, 181 (1991).
2. P. R. Weissman, in *Protostars and Planets II*, Ed. by D. C. Black and M. S. Mattwesw, (Univ. of Arizona Press, Tucson, 1984), p. 895.
3. C. M. Telesco, E. E. Becklin, R. D. Wolstencroft, and R. Decher, Nature **335**, 51 (1988).
4. W. H. Sorrell, Astrophys. J. **361**, 150 (1990).
5. V. P. Grinin, N. N. Kiselev, N. Kh. Minikulov, *et al.*, Astrophys. Space Sci. **186**, 283 (1991).
6. V. N. Voshchinnikov, F. J. Molster, and P. S. Thé, Astron. Astrophys. **312**, 243 (1996).
7. A. Miroshnichenko, Z. Ivezic, and M. Elitzur, Astrophys. J. Lett. **475**, L41 (1997).
8. S. Pezzuto, F. Strafella, and D. Lorenzetti, Astrophys. J. **485**, 290 (1997).
9. Th. Henning, in *Molecules in Astrophysics: Probes and Processes*, Ed. by E. F. van Dishoeck (Kluwer, 1997), p. 343.
10. E. Pantin, P. O. Lagage, and P. Artymowicz, Astron. Astrophys. **327**, 1123 (1997).
11. A. Li and J. M. Greenberg, Astron. Astrophys. **331**, 291 (1998).
12. N. A. Krivova and V. B. Il'in, Pis'ma Astron. Zh. **23**, 908 (1997) [Astron. Lett. **23**, 791 (1997)].
13. J. S. Mathis, W. Rumpl, and K. H. Nordsieck, Astrophys. J. **217**, 425 (1977).
14. B. T. Draine, ASP Conf. Ser. **58**, 227 (1994).
15. J. S. Mathis, Astrophys. J. **497**, 824 (1998).
16. C. F. Bohren and D. R. Huffman, *Absorption and Scattering of Light by Small Particles* (Wiley, New York, 1983; Mir, Moscow, 1986).
17. A. Laor and B. T. Draine, Astrophys. J. **402**, 441 (1993).
18. R. Stongnienko, Th. Henning, and V. Ossenkopf, Astron. Astrophys. **296**, 797 (1995).
19. M. J. Wolff, G. C. Clayton, and S. J. Gibson, Astrophys. J. **503**, 815 (1998).
20. O. Fischer, Rev. Mod. Astron. **8**, 103 (1995).
21. N. A. Krivova, Candidate's Dissertation (St. Petersburg Univ., St. Petersburg, 1998).
22. R. Chini, E. Krügel, and E. Kreysa, Astron. Astrophys. **167**, 315 (1986).
23. P. S. Thé, D. de Winter, and M. R. Pérez, Astron. Astrophys., Suppl. Ser. **104**, 315 (1994).
24. V. P. Grinin, ASP Conf. Ser. **62**, 63 (1994).
25. V. P. Grinin, Pis'ma Astron. Zh. **14**, 65 (1988).
26. G. V. Zaitseva and V. M. Lyuty, Pis'ma Astron. Zh. **23**, 277 (1997) [Astron. Lett. **23**, 242 (1997)].
27. N. A. Krivova, V. B. Il'in, and O. Fischer, Publ. NASA **3343**, 37 (1996).
28. N. A. Krivova, Pis'ma Astron. Zh. **23**, 371 (1997) [Astron. Lett. **23**, 327 (1997)].
29. C. Friedemann, H.- G. Reimann, J. Gürtler, and V. Tóth, Astron. Astrophys. **277**, 184 (1993).
30. Z. Ivezic and M. Elitzur, Mon. Not. R. Astron. Soc. **287**, 799 (1997).

31. J. I. Hage and J. M. Greenberg, Astrophys. J. **361**, 251 (1990).
32. V. Ossenkopf, Astron. Astrophys. **251**, 210 (1991).
33. Th. Henning and R. Stognienko, Astron. Astrophys. **280**, 609 (1993).
34. J. S. Mathis, Astrophys. J. **472**, 643 (1996).
35. H. R. E. Tjin A Djie, L. Remijn, and P. S. Thé, Astron. Astrophys. **134**, 273 (1984).
36. A. V. Berdyugin, V. P. Grinin, and N. Kh. Minikulov, Izv. Krymsk. Astrofiz. Obs. **86**, 69 (1992).
37. A. Witt, in *Interstellar Dust. IAU Symp. No. 135*, Ed. by L. J. Allamandola and A. G. G. M. Tielens (Reidel, Dordrecht, 1989), p. 87.
38. F. Berrilli, G. Corciulo, G. Ingrosso, *et al.*, Astrophys. J. **398**, 254 (1992).
39. A. Natta, J. Prusti, and E. Krügel, Astron. Astrophys. **275**, 572 (1993).
40. A. S. Mitskevitch, Astron. Astrophys. **298**, 219 (1995).
41. A. S. Mitskevitch, Astron. Astrophys. **298**, 231 (1995).
42. N. V. Voshchinnikov and V. V. Karjukin, Astron. Astrophys. **288**, 883 (1994).
43. H. Kimura and I. Mann, J. Quant. Spectroscop. Radiat. Transf. **60**, 425 (1998).
44. N. A. Krivova and V. B. Il'in, Icarus, 1999 (in press).
45. V. B. Il'in and N. V. Voshchinnikov, Astron. Zh. **70**, 721 (1993).
46. V. B. Il'in and A. V. Krivov, ASP Conf. Ser. **62**, 177 (1994).
47. T. Mukai, H. Ishimoto, T. Kozasa, *et al.*, Astron. Astrophys. **262**, 315 (1992).
48. P. Artymowicz, Astrophys. J. Lett. **335**, L79 (1988).
49. P. L. Lamy and J.-M. Perrin, Astron. Astrophys. **327**, 1147 (1997).
50. C. Jäger, H. Mutschke, B. Begemann, *et al.*, Astron. Astrophys. **292**, 641 (1994).
51. T. Kozasa, J. Blum, and T. Mukai, Astron. Astrophys. **263**, 423 (1992).
52. T. Kozasa, J. Blum, H. Okamoto, and T. Mukai, Astron. Astrophys. **276**, 278 (1993).
53. B. T. Draine, Astrophys. J. **333**, 848 (1988).
54. M. Cohen, Mon. Not. R. Astron. Soc. **161**, 97 (1973).
55. I. S. Glass and M. V. Penston, Mon. Not. R. Astron. Soc. **167**, 237 (1974).
56. E. A. Kolotilov, Astrofizika **13**, 33 (1977).
57. W. B. Weaver and G. Jones, Astrophys. J., Suppl. Ser. **78**, 239 (1992).
58. W. Li, N. J. Evans II, P. M. Harvey, and C. Colomé, Astrophys. J. **433**, 199 (1994).

Translated by V. Astakhov